

Frustum PointNets for 3D Object Detection from RGB-D Data

Charles R. Qi^{1*} Wei Liu² Chenxia Wu² Hao Su³ Leonidas J. Guibas¹
¹Stanford University ²Nuro, Inc. ³UC San Diego

Abstract

In this work, we study 3D object detection from RGB-D data in both indoor and outdoor scenes. While previous methods focus on images or 3D voxels, often obscuring natural 3D patterns and invariances of 3D data, we directly operate on raw point clouds by popping up RGB-D scans. However, a key challenge of this approach is how to efficiently localize objects in point clouds of large-scale scenes (region proposal). Instead of solely relying on 3D proposals, our method leverages both mature 2D object detectors and advanced 3D deep learning for object localization, achieving efficiency as well as high recall for even small objects. Benefited from learning directly in raw point clouds, our method is also able to precisely estimate 3D bounding boxes even under strong occlusion or with very sparse points. Evaluated on KITTI and SUN RGB-D 3D detection benchmarks, our method outperforms the state of the art by remarkable margins while having real-time capability.

1. Introduction

Recently, great progress has been made on 2D image understanding tasks, such as object detection [10] and instance segmentation [11]. However, beyond getting 2D bounding boxes or pixel masks, 3D understanding is eagerly in demand in many applications such as autonomous driving and augmented reality (AR). With the popularity of 3D sensors deployed on mobile devices and autonomous vehicles, more and more 3D data is captured and processed. In this work, we study one of the most important 3D perception tasks – 3D object detection, which classifies the object category and estimates *oriented 3D bounding boxes* of physical objects from 3D sensor data.

While 3D sensor data is often in the form of point clouds, how to represent point cloud and what deep net architectures to use for 3D object detection remains an open problem. Most existing works convert 3D point clouds to images by projection [30, 21] or to volumetric grids by quantization [33, 18, 21] and then apply convolutional networks.

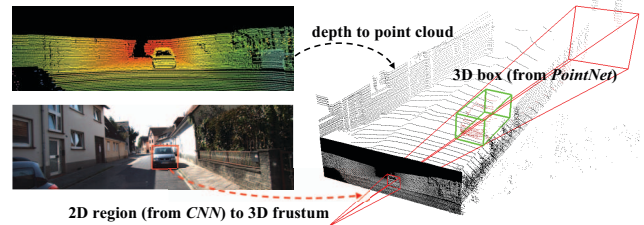


Figure 1. **3D object detection pipeline.** Given RGB-D data, we first generate 2D object region proposals in the RGB image using a CNN. Each 2D region is then extruded to a 3D viewing frustum in which we get a point cloud from depth data. Finally, our frustum PointNet predicts a (oriented and amodal) 3D bounding box for the object from the points in frustum.

This data representation transformation, however, may obscure natural 3D patterns and invariances of the data. Recently, a number of papers have proposed to process point clouds directly without converting them to other formats. For example, [20, 22] proposed new types of deep net architectures, called *PointNets*, which have shown superior performance and efficiency in several 3D understanding tasks such as object classification and semantic segmentation.

While PointNets are capable of classifying a whole point cloud or predicting a semantic class for each point in a point cloud, it is unclear how this architecture can be used for instance-level 3D object detection. Towards this goal, we have to address one key challenge: how to efficiently propose possible locations of 3D objects in a 3D space. Imitating the practice in image detection, it is straightforward to enumerate candidate 3D boxes by sliding windows [7] or by 3D region proposal networks such as [27]. However, the computational complexity of 3D search typically grows cubically with respect to resolution and becomes too expensive for large scenes or real-time applications such as autonomous driving.

Instead, in this work, we reduce the search space following the dimension reduction principle: we take the advantage of mature 2D object detectors (Fig. 1). First, we extract the 3D bounding frustum of an object by extruding 2D bounding boxes from image detectors. Then, within the 3D space trimmed by each of the 3D frustums, we consecutively perform 3D object instance segmentation and *amodal*

*Majority of the work done as an intern at Nuro, Inc.

3D bounding box regression using two variants of PointNet. The segmentation network predicts the 3D mask of the object of interest (i.e. instance segmentation); and the regression network estimates the amodal 3D bounding box (covering the entire object even if only part of it is visible).

In contrast to previous work that treats RGB-D data as 2D maps for CNNs, our method is more *3D-centric* as we lift depth maps to 3D point clouds and process them using 3D tools. This 3D-centric view enables new capabilities for exploring 3D data in a more effective manner. First, in our pipeline, a few transformations are applied successively on 3D coordinates, which align point clouds into a sequence of more constrained and canonical frames. These alignments factor out pose variations in data, and thus make 3D geometry pattern more evident, leading to an easier job of 3D learners. Second, learning in 3D space can better exploits the geometric and topological structure of 3D space. In principle, all objects live in 3D space; therefore, we believe that many geometric structures, such as repetition, planarity, and symmetry, are more naturally parameterized and captured by learners that directly operate in 3D space. The usefulness of this 3D-centric network design philosophy has been supported by much recent experimental evidence.

Our method achieve leading positions on KITTI 3D object detection [1] and bird’s eye view detection [2] benchmarks. Compared with the previous state of the art [5], our method is 8.04% better on 3D car AP with high efficiency (running at 5 fps). Our method also fits well to indoor RGB-D data where we have achieved 8.9% and 6.4% better 3D mAP than [13] and [24] on SUN-RGBD while running one to three orders of magnitude faster.

The key contributions of our work are as follows:

- We propose a novel framework for RGB-D data based 3D object detection called Frustum PointNets.
- We show how we can train 3D object detectors under our framework and achieve state-of-the-art performance on standard 3D object detection benchmarks.
- We provide extensive quantitative evaluations to validate our design choices as well as rich qualitative results for understanding the strengths and limitations of our method.

2. Related Work

3D Object Detection from RGB-D Data Researchers have approached the 3D detection problem by taking various ways to represent RGB-D data.

Front view image based methods: [3, 19, 34] take monocular RGB images and shape priors or occlusion patterns to infer 3D bounding boxes. [15, 6] represent depth data as 2D maps and apply CNNs to localize objects in 2D image. In comparison we represent depth as a point cloud

and use advanced 3D deep networks (PointNets) that can exploit 3D geometry more effectively.

Bird’s eye view based methods: MV3D [5] projects LiDAR point cloud to bird’s eye view and trains a region proposal network (RPN [23]) for 3D bounding box proposal. However, the method lags behind in detecting small objects, such as pedestrians and cyclists and cannot easily adapt to scenes with multiple objects in vertical direction.

3D based methods: [31, 28] train 3D object classifiers by SVMs on hand-designed geometry features extracted from point cloud and then localize objects using sliding-window search. [7] extends [31] by replacing SVM with 3D CNN on voxelized 3D grids. [24] designs new geometric features for 3D object detection in a point cloud. [29, 14] convert a point cloud of the entire scene into a volumetric grid and use 3D volumetric CNN for object proposal and classification. Computation cost for those method is usually quite high due to the expensive cost of 3D convolutions and large 3D search space. Recently, [13] proposes a 2D-driven 3D object detection method that is similar to ours in spirit. However, they use hand-crafted features (based on histogram of point coordinates) with simple fully connected networks to regress 3D box location and pose, which is sub-optimal in both speed and performance. In contrast, we propose a more flexible and effective solution with deep 3D feature learning (PointNets).

Deep Learning on Point Clouds Most existing works convert point clouds to images or volumetric forms before feature learning. [33, 18, 21] voxelize point clouds into volumetric grids and generalize image CNNs to 3D CNNs. [16, 25, 32, 7] design more efficient 3D CNN or neural network architectures that exploit sparsity in point cloud. However, these CNN based methods still require quantization of point clouds with certain voxel resolution. Recently, a few works [20, 22] propose a novel type of network architectures (PointNets) that directly consumes raw point clouds without converting them to other formats. While PointNets have been applied to single object classification and semantic segmentation, our work explores how to extend the architecture for the purpose of 3D object detection.

3. Problem Definition

Given RGB-D data as input, our goal is to classify and localize objects in 3D space. The depth data, obtained from LiDAR or indoor depth sensors, is represented as a point cloud in RGB camera coordinates. The projection matrix is also known so that we can get a 3D frustum from a 2D image region. Each object is represented by a class (one among k predefined classes) and an *amodal* 3D bounding box. The *amodal* box bounds the complete object even if part of the object is occluded or truncated. The 3D box is

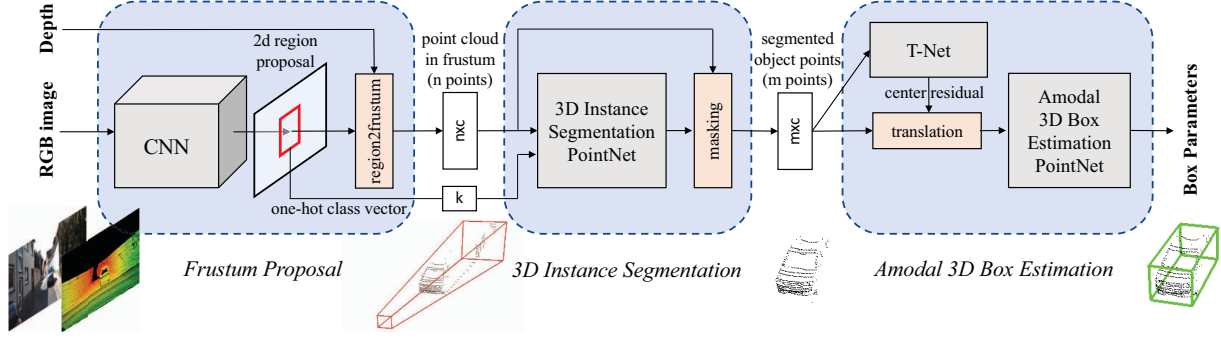


Figure 2. **Frustum PointNets for 3D object detection.** We first leverage a 2D CNN object detector to propose 2D regions and classify their content. 2D regions are then lifted to 3D and thus become frustum proposals. Given a point cloud in a frustum ($n \times c$ with n points and c channels of XYZ, intensity etc. for each point), the object instance is segmented by binary classification of each point. Based on the segmented object point cloud ($m \times c$), a light-weight regression PointNet (T-Net) tries to align points by translation such that their centroid is close to amodal box center. At last the box estimation net estimates the amodal 3D bounding box for the object. More illustrations on coordinate systems involved and network input, output are in Fig. 4 and Fig. 5.

parameterized by its size h, w, l , center c_x, c_y, c_z , and orientation θ, ϕ, ψ relative to a predefined canonical pose for each category. In our implementation, we only consider the heading angle θ around the up-axis for orientation.

4. 3D Detection with Frustum PointNets

As shown in Fig. 2, our system for 3D object detection consists of three modules: frustum proposal, 3D instance segmentation, and 3D amodal bounding box estimation. We will introduce each module in the following subsections. We will focus on the pipeline and functionality of each module, and refer readers to supplementary for specific architectures of the deep networks involved.

4.1. Frustum Proposal

The resolution of data produced by most 3D sensors, especially real-time depth sensors, is still lower than RGB images from commodity cameras. Therefore, we leverage mature 2D object detector to propose 2D object regions in RGB images as well as to classify objects.

With a known camera projection matrix, a 2D bounding box can be lifted to a frustum (with near and far planes specified by depth sensor range) that defines a 3D search space for the object. We then collect all points within the frustum to form a *frustum point cloud*. As shown in Fig 4 (a), frustums may orient towards many different directions, which result in large variation in the placement of point clouds. We therefore normalize the frustums by rotating them toward a center view such that the center axis of the frustum is orthogonal to the image plane. This normalization helps improve the rotation-invariance of the algorithm. We call this entire procedure for extracting frustum point clouds from RGB-D data *frustum proposal generation*.

While our 3D detection framework is agnostic to the exact method for 2D region proposal, we adopt a FPN [17]

based model. We pre-train the model weights on ImageNet classification and COCO object detection datasets and further fine-tune it on a KITTI 2D object detection dataset to classify and predict *amodal* 2D boxes. More details of the 2D detector training are provided in the supplementary.

4.2. 3D Instance Segmentation

Given a 2D image region (and its corresponding 3D frustum), several methods might be used to obtain 3D location of the object: One straightforward solution is to directly regress 3D object locations (e.g., by 3D bounding box) from a depth map using 2D CNNs. However, this problem is not easy as occluding objects and background clutter is common in natural scenes (as in Fig. 3), which may severely distract the 3D localization task. Because objects are naturally separated in physical space, segmentation in 3D point cloud is much more natural and easier than that in images where pixels from distant objects can be near-by to each other. Having observed this fact, we propose to seg-

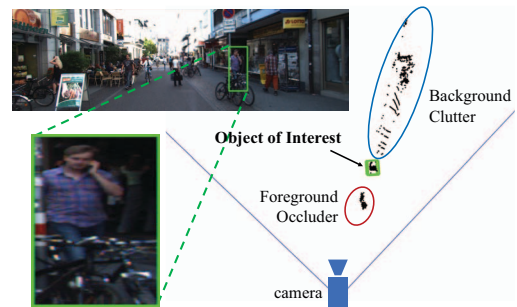


Figure 3. **Challenges for 3D detection in frustum point cloud.** Left: RGB image with an image region proposal for a person. Right: bird's eye view of the LiDAR points in the extruded frustum from 2D box, where we see a wide spread of points with both foreground occluder (bikes) and background clutter (building).

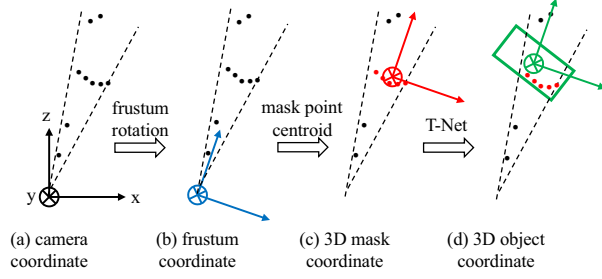


Figure 4. **Coordinate systems for point cloud.** Artificial points (black dots) are shown to illustrate (a) default camera coordinate; (b) frustum coordinate after rotating frustums to center view (Sec. 4.1); (c) mask coordinate with object points’ centroid at origin (Sec. 4.2); (d) object coordinate predicted by T-Net (Sec. 4.3).

ment instances in 3D point cloud instead of in 2D image or depth map. Similar to Mask-RCNN [11], which achieves instance segmentation by binary classification of pixels in image regions, we realize 3D instance segmentation using a PointNet-based network on point clouds in frustums.

Based on 3D instance segmentation, we are able to achieve *residual* based 3D localization. That is, rather than regressing the absolute 3D location of the object whose offset from the sensor may vary in large ranges (e.g. from 5m to beyond 50m in KITTI data), we predict the 3D bounding box center in a local coordinate system – 3D mask coordinates as shown in Fig. 4 (c).

3D Instance Segmentation PointNet. The network takes a point cloud in frustum and predicts a probability score for each point that indicates how likely the point belongs to the object of interest. Note that each frustum contains exactly one object of interest. Here those “other” points could be points of non-relevant areas (such as ground, vegetation) or other instances that occlude or are behind the object of interest. Similar to the case in 2D instance segmentation, depending on the position of the frustum, object points in one frustum may become cluttered or occlude points in another. Therefore, our segmentation PointNet is learning the occlusion and clutter patterns as well as recognizing the geometry for the object of a certain category.

In a multi-class detection case, we also leverage the semantics from a 2D detector for better instance segmentation. For example, if we know the object of interest is a pedestrian, then the segmentation network can use this prior to find geometries that look like a person. Specifically, in our architecture we encode the semantic category as a one-hot class vector (k dimensional for the pre-defined k categories) and concatenate the one-hot vector to the intermediate point cloud features. More details of the specific architectures are described in the supplementary.

After 3D instance segmentation, points that are classified as the object of interest are extracted (“masking” in Fig. 2).

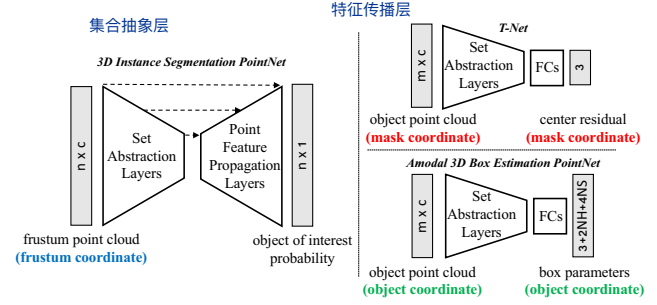


Figure 5. **Basic architectures and IO for PointNets.** Architecture is illustrated for PointNet++ [22] (v2) models with set abstraction layers and feature propagation layers (for segmentation). Coordinate systems involved are visualized in Fig. 4.

Having obtained these segmented object points, we further normalize its coordinates to boost the translational invariance of the algorithm, following the same rationale as in the frustum proposal step. In our implementation, we transform the point cloud into a local coordinate by subtracting XYZ values by its centroid. This is illustrated in Fig. 4 (c). Note that we intentionally do not scale the point cloud, because the bounding sphere size of a partial point cloud can be greatly affected by viewpoints and the real size of the point cloud helps the box size estimation.

In our experiments, we find that coordinate transformations such as the one above and the previous frustum rotation are critical for 3D detection result as shown in Tab. 8.

4.3. Amodal 3D Box Estimation

Given the segmented object points (in 3D mask coordinate), this module estimates the object’s amodal oriented 3D bounding box by using a box regression PointNet together with a preprocessing transformer network.

Learning-based 3D Alignment by T-Net Even though we have aligned segmented object points according to their centroid position, we find that the origin of the mask coordinate frame (Fig. 4 (c)) may still be quite far from the *amodal* box center. We therefore propose to use a light-weight regression PointNet (T-Net) to estimate the true center of the complete object and then transform the coordinate such that the predicted center becomes the origin (Fig. 4 (d)).

The architecture and training of our T-Net is similar to the T-Net in [20], which can be thought of as a special type of spatial transformer network (STN) [12]. However, different from the original STN that has no direct supervision on transformation, we explicitly supervise our translation network to predict center residuals from the mask coordinate origin to real object center.

Amodal 3D Box Estimation PointNet The box estimation network predicts amodal bounding boxes (for entire

object even if part of it is unseen) for objects given an object point cloud in 3D object coordinate (Fig. 4 (d)). The network architecture is similar to that for object classification [20, 22], however the output is no longer object class scores but parameters for a 3D bounding box.

As stated in Sec. 3, we parameterize a 3D bounding box by its center (c_x, c_y, c_z) , size (h, w, l) and heading angle θ (along up-axis). We take a “residual” approach for box center estimation. The center residual predicted by the box estimation network is combined with the previous center residual from the T-Net and the masked points’ centroid to recover an absolute center (Eq. 1). For box size and heading angle, we follow previous works [23, 19] and use a hybrid of classification and regression formulations. Specifically we pre-define NS size templates and NH equally split angle bins. Our model will both classify size/heading (NS scores for size, NH scores for heading) to those pre-defined categories as well as predict residual numbers for each category ($3 \times NS$ residual dimensions for height, width, length, NH residual angles for heading). In the end the net outputs $3 + 4 \times NS + 2 \times NH$ numbers in total.

$$C_{pred} = C_{mask} + \Delta C_{t-net} + \Delta C_{box-net} \quad (1)$$

4.4. Training with Multi-task Losses

We simultaneously optimize the three nets involved (3D instance segmentation PointNet, T-Net and amodal box estimation PointNet) with multi-task losses (as in Eq. 2). L_{c1-reg} is for T-Net and L_{c2-reg} is for center regression of box estimation net. L_{h-cls} and L_{h-reg} are losses for heading angle prediction while L_{s-cls} and L_{s-reg} are for box size. Softmax is used for all classification tasks and smooth- l_1 (huber) loss is used for all regression cases.

$$L_{multi-task} = L_{seg} + \lambda(L_{c1-reg} + L_{c2-reg} + L_{h-cls} + L_{h-reg} + L_{s-cls} + L_{s-reg} + \gamma L_{corner}) \quad (2)$$

Corner Loss for Joint Optimization of Box Parameters

While our 3D bounding box parameterization is compact and complete, learning is not optimized for final 3D box accuracy – center, size and heading have *separate* loss terms. Imagine cases where center and size are accurately predicted but heading angle is off – the 3D IoU with ground truth box will then be dominated by the angle error. Ideally all three terms (center, size, heading) should be *jointly* optimized for best 3D box estimation (under IoU metric). To resolve this problem we propose a novel regularization loss, the *corner loss*:

$$L_{corner} = \sum_{i=1}^{NS} \sum_{j=1}^{NH} \delta_{ij} \min \left\{ \sum_{k=1}^8 \|P_k^{ij} - P_k^*\|, \sum_{i=1}^8 \|P_k^{ij} - P_k^{**}\| \right\} \quad (3)$$

In essence, the corner loss is the sum of the distances between the eight corners of a predicted box and a ground truth box. Since corner positions are jointly determined by center, size and heading, the corner loss is able to regularize the multi-task training for those parameters.

To compute the corner loss, we firstly construct $NS \times NH$ “anchor” boxes from all size templates and heading angle bins. The anchor boxes are then translated to the estimated box center. We denote the anchor box corners as P_k^{ij} , where i, j, k are indices for the size class, heading class, and (predefined) corner order, respectively. To avoid large penalty from flipped heading estimation, we further compute distances to corners (P_k^{**}) from the flipped ground truth box and use the minimum of the original and flipped cases. δ_{ij} , which is one for the ground truth size/heading class and zero else wise, is a two-dimensional mask used to select the distance term we care about.

5. Experiments

Experiments are divided into three parts¹. First we compare with state-of-the-art methods for 3D object detection on KITTI [8] and SUN-RGBD [27] (Sec 5.1). Second, we provide in-depth analysis to validate our design choices (Sec 5.2). Last, we show qualitative results and discuss the strengths and limitations of our methods (Sec 5.3).

5.1. Comparing with state-of-the-art Methods

We evaluate our 3D object detector on KITTI [9] and SUN-RGBD [27] benchmarks for 3D object detection. On both tasks we have achieved significantly better results compared with state-of-the-art methods.

KITTI Tab. 1 shows the performance of our 3D detector on the KITTI *test* set. We outperform previous state-of-the-art methods by a large margin. While MV3D [5] uses multi-view feature aggregation and sophisticated multi-sensor fusion strategy, our method based on the PointNet [20] (v1) and PointNet++ [22] (v2) backbone is much cleaner in design. While out of the scope for this work, we expect that sensor fusion (esp. aggregation of image feature for 3D detection) could further improve our results.

We also show our method’s performance on 3D object localization (bird’s eye view) in Tab. 2. In the 3D localization task bounding boxes are projected to bird’s eye view plane and IoU is evaluated on oriented 2D boxes. Again, our method significantly outperforms previous works which include DoBEM [35] and MV3D [5] that use CNNs on projected LiDAR images, as well as 3D FCN [14] that uses 3D CNNs on voxelized point cloud.

¹Details on network architectures, training parameters as well as more experiments are included in the supplementary material.

| Method | Cars | | | Pedestrians | | | Cyclists | | |
|------------|--------------|--------------|--------------|--------------|--------------|--------------|--------------|--------------|--------------|
| | Easy | Moderate | Hard | Easy | Moderate | Hard | Easy | Moderate | Hard |
| DoBEM [35] | 7.42 | 6.95 | 13.45 | - | - | - | - | - | - |
| MV3D [5] | 71.09 | 62.35 | 55.12 | - | - | - | - | - | - |
| Ours (v1) | 80.62 | 64.70 | 56.07 | 50.88 | 41.55 | 38.04 | 69.36 | 53.50 | 52.88 |
| Ours (v2) | 81.20 | 70.39 | 62.19 | 51.21 | 44.89 | 40.23 | 71.96 | 56.77 | 50.39 |

Table 1. **3D object detection** 3D AP on KITTI *test* set. DoBEM [35] and MV3D [5] (previous state of the art) are based on 2D CNNs with bird’s eye view LiDAR image. Our method, without sensor fusion or multi-view aggregation, outperforms those methods by large margins on all categories and data subsets. 3D bounding box IoU threshold is 70% for cars and 50% for pedestrians and cyclists.

| Method | Cars | | | Pedestrians | | | Cyclists | | |
|-------------|--------------|--------------|--------------|--------------|--------------|--------------|--------------|--------------|--------------|
| | Easy | Moderate | Hard | Easy | Moderate | Hard | Easy | Moderate | Hard |
| DoBEM [35] | 36.49 | 36.95 | 38.10 | - | - | - | - | - | - |
| 3D FCN [14] | 69.94 | 62.54 | 55.94 | - | - | - | - | - | - |
| MV3D [5] | 86.02 | 76.90 | 68.49 | - | - | - | - | - | - |
| Ours (v1) | 87.28 | 77.09 | 67.90 | 55.26 | 47.56 | 42.57 | 73.42 | 59.87 | 52.88 |
| Ours (v2) | 88.70 | 84.00 | 75.33 | 58.09 | 50.22 | 47.20 | 75.38 | 61.96 | 54.68 |

Table 2. **3D object localization** AP (bird’s eye view) on KITTI *test* set. 3D FCN [14] uses 3D CNNs on voxelized point cloud and is far from real-time. MV3D [5] is the previous state of the art. Our method significantly outperforms those methods on all categories and data subsets. Bird’s eye view 2D bounding box IoU threshold is 70% for cars and 50% for pedestrians and cyclists.

| Method | Easy | Moderate | Hard |
|------------------|--------------|--------------|--------------|
| Mono3D [3] | 2.53 | 2.31 | 2.31 |
| 3DOP [4] | 6.55 | 5.07 | 4.10 |
| VeloFCN [14] | 15.20 | 13.66 | 15.98 |
| MV3D (LiDAR) [5] | 71.19 | 56.60 | 55.30 |
| MV3D [5] | 71.29 | 62.68 | 56.56 |
| Ours (v1) | 83.26 | 69.28 | 62.56 |
| Ours (v2) | 83.76 | 70.92 | 63.65 |

Table 3. **3D object detection** AP on KITTI *val* set (cars only).

| Method | Easy | Moderate | Hard |
|------------------|--------------|--------------|--------------|
| Mono3D [3] | 5.22 | 5.19 | 4.13 |
| 3DOP [4] | 12.63 | 9.49 | 7.59 |
| VeloFCN [14] | 40.14 | 32.08 | 30.47 |
| MV3D (LiDAR) [5] | 86.18 | 77.32 | 76.33 |
| MV3D [5] | 86.55 | 78.10 | 76.67 |
| Ours (v1) | 87.82 | 82.44 | 74.77 |
| Ours (v2) | 88.16 | 84.02 | 76.44 |

Table 4. **3D object localization** AP on KITTI *val* set (cars only).

The output of our network is visualized in Fig. 6 where we observe accurate 3D instance segmentation and box prediction even under very challenging cases. We defer more discussions on success and failure case patterns to Sec. 5.3. We also report performance on KITTI *val* set (the same split as in [5]) in Tab. 3 and Tab. 4 (for cars) to support comparison with more published works, and in Tab. 5 (for pedestrians and cyclists) for reference.

SUN-RGBD Most previous 3D detection works specialize either on outdoor LiDAR scans where objects are well separated in space and the point cloud is sparse (so that it’s feasible for bird’s eye projection), or on indoor depth maps that are regular images with dense pixel values such

| Benchmark | Easy | Moderate | Hard |
|------------------------------|-------|----------|-------|
| Pedestrian (3D Detection) | 70.00 | 61.32 | 53.59 |
| Pedestrian (Bird’s Eye View) | 72.38 | 66.39 | 59.57 |
| Cyclist (3D Detection) | 77.15 | 56.49 | 53.37 |
| Cyclist (Bird’s Eye View) | 81.82 | 60.03 | 56.32 |

Table 5. Performance on KITTI *val* set for pedestrians and cyclists. Model evaluated is Ours (v2).

that image CNNs can be easily applied. However, methods designed for bird’s eye view may be incapable for indoor rooms where multiple objects often exist together in vertical space. On the other hand, indoor focused methods could find it hard to apply to sparse and large-scale point cloud from LiDAR scans.

In contrast, our frustum-based PointNet is a generic framework for both outdoor and indoor 3D object detection. By applying the same pipeline we used for KITTI data set, we’ve achieved state-of-the-art performance on SUN-RGBD benchmark (Tab. 6) with significantly higher mAP as well as much faster (10x-1000x) inference speed.

5.2. Architecture Design Analysis

In this section we provide analysis and ablation experiments to validate our design choices.

Experiment setup. Unless otherwise noted, all experiments in this section are based on our v1 model on KITTI data using train/val split as in [5]. To decouple the influence of 2D detectors, we use ground truth 2D boxes for region proposals and use 3D box estimation accuracy (IoU threshold 0.7) as the evaluation metric. We will only focus on the car category which has the most training examples.

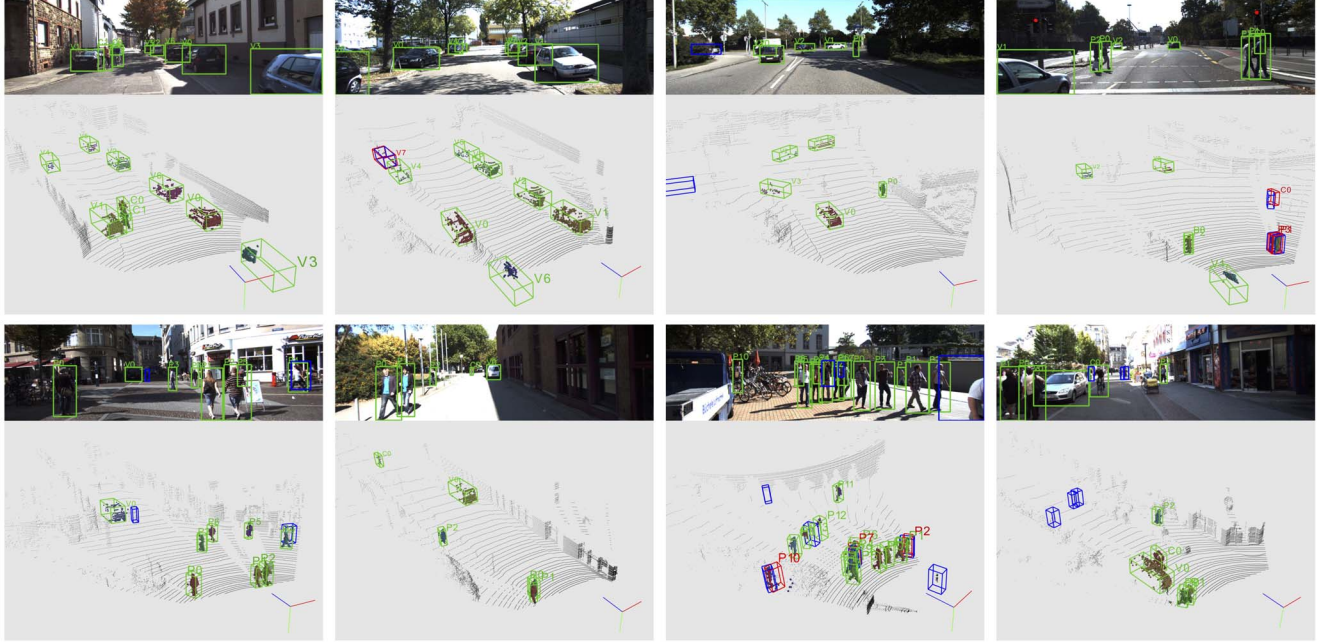


Figure 6. **Visualizations of Frustum PointNet results on KITTI val set** (best viewed in color with zoom in). These results are based on PointNet++ models [22], running at 5 fps and achieving test set 3D AP of 70.39, 44.89 and 56.77 for car, pedestrian and cyclist, respectively. 3D instance masks on point cloud are shown in color. True positive detection boxes are in green, while false positive boxes are in red and groundtruth boxes in blue are shown for false positive and false negative cases. Digit and letter beside each box denote instance id and semantic class, with “v” for cars, “p” for pedestrian and “c” for cyclist. See Sec. 5.3 for more discussion on the results.

| | bathtub | bed | bookshelf | chair | desk | dresser | nightstand | sofa | table | toilet | Runtime | mAP |
|----------------|-------------|-------------|-------------|-------------|-------------|-------------|-------------|-------------|-------------|-------------|----------|-------------|
| DSS [29] | 44.2 | 78.8 | 11.9 | 61.2 | 20.5 | 6.4 | 15.4 | 53.5 | 50.3 | 78.9 | 19.55s | 42.1 |
| COG [24] | 58.3 | 63.7 | 31.8 | 62.2 | 45.2 | 15.5 | 27.4 | 51.0 | 51.3 | 70.1 | 10-30min | 47.6 |
| 2D-driven [13] | 43.5 | 64.5 | 31.4 | 48.3 | 27.9 | 25.9 | 41.9 | 50.4 | 37.0 | 80.4 | 4.15s | 45.1 |
| Ours (v1) | 43.3 | 81.1 | 33.3 | 64.2 | 24.7 | 32.0 | 58.1 | 61.1 | 51.1 | 90.9 | 0.12s | 54.0 |

Table 6. **3D object detection AP on SUN-RGBD val set.** Evaluation metric is average precision with 3D IoU threshold 0.25 as proposed by [27]. Note that both COG [24] and 2D-driven [13] use room layout context to boost performance while ours and DSS [29] not. Compared with previous state-of-the-arts our method is 6.4% to 11.9% better in mAP as well as one to three orders of magnitude faster.

Comparing with alternative approaches for 3D detection. In this part we evaluate a few CNN-based baseline approaches as well as ablated versions and variants of our pipelines using 2D masks. In the first row of Tab. 7, we show 3D box estimation results from two CNN-based networks. The baseline methods trained VGG [26] models on ground truth boxes of RGB-D images and adopt the same box parameter and loss functions as our main method. While the model in the first row directly estimates box location and parameters from vanilla RGB-D image patch, the other one (second row) uses a FCN trained from the COCO dataset for 2D mask estimation (as that in Mask-RCNN [11]) and only uses features from the masked region for prediction. The depth values are also translated by subtracting the median depth within the 2D mask. However, both CNN baselines get far worse results compared to our main method.

To understand why CNN baselines underperform, we vi-

sualize a typical 2D mask prediction in Fig. 7. While the estimated 2D mask appears in high quality on an RGB image, there are still lots of clutter and foreground points in the 2D mask. In comparison, our 3D instance segmentation gets much cleaner result, which greatly eases the next module in finer localization and bounding box regression.

In the third row of Tab. 7, we experiment with an ablated version of frustum PointNet that has no 3D instance segmentation module. Not surprisingly, the model gets much worse results than our main method, which indicates the critical effect of our 3D instance segmentation module. In the fourth row, instead of 3D segmentation we use point clouds from 2D masked depth maps (Fig. 7) for 3D box estimation. However, since a 2D mask is not able to cleanly segment the 3D object, the performance is more than 12% worse than that with the 3D segmentation (our main method in the fifth row). On the other hand, a combined usage of 2D and 3D masks – applying 3D segmentation on point cloud

| network arch. | mask | depth representation | accuracy |
|---------------|-------|----------------------|-------------|
| ConvNet | - | image | 18.3 |
| ConvNet | 2D | image | 27.4 |
| PointNet | - | point cloud | 33.5 |
| PointNet | 2D | point cloud | 61.6 |
| PointNet | 3D | point cloud | 74.3 |
| PointNet | 2D+3D | point cloud | 70.0 |

Table 7. **Comparing 2D and 3D approaches.** 2D mask is from FCN on RGB image patch. 3D mask is from PointNet on frustum point cloud. 2D+3D mask is 3D mask generated by PointNet on point cloud popped up from 2D masked depth map.

| frustum rot. | mask centralize | t-net | accuracy |
|--------------|-----------------|-------|-------------|
| - | - | - | 12.5 |
| ✓ | - | - | 48.1 |
| - | ✓ | - | 64.6 |
| ✓ | ✓ | - | 71.5 |
| ✓ | ✓ | ✓ | 74.3 |

Table 8. **Effects of point cloud normalization.** Metric is 3D box estimation accuracy with IoU=0.7.

| loss type | regularization | accuracy |
|----------------------|----------------|-------------|
| regression only | - | 62.9 |
| cls-reg | - | 71.8 |
| cls-reg (normalized) | - | 72.2 |
| cls-reg (normalized) | corner loss | 74.3 |

Table 9. **Effects of 3D box loss formulations.** Metric is 3D box estimation accuracy with IoU=0.7.

from 2D masked depth map – also shows slightly worse results than our main method probably due to the accumulated error from inaccurate 2D mask predictions.

Effects of point cloud normalization. As shown in Fig. 4, our frustum PointNet takes a few key coordinate transformations to canonicalize the point cloud for more effective learning. Tab. 8 shows how each normalization step helps for 3D detection. We see that both frustum rotation (such that frustum points have more similar XYZ distributions) and mask centroid subtraction (such that object points have smaller and more canonical XYZ) are critical. In addition, extra alignment of object point cloud to object center by T-Net also contributes significantly to the performance.

Effects of regression loss formulation and corner loss. In Tab. 9 we compare different loss options and show that a combination of “cls-reg” loss (the classification and residual regression approach for heading and size regression) and a regularizing corner loss achieves the best result.

The naive baseline using regression loss only (first row) achieves unsatisfactory result because the regression target is large in range (object size from 0.2m to 5m). In comparison, the cls-reg loss and a normalized version (residual normalized by heading bin size or template shape size) of it achieve much better performance. At last row we show that a regularizing corner loss further helps optimization.

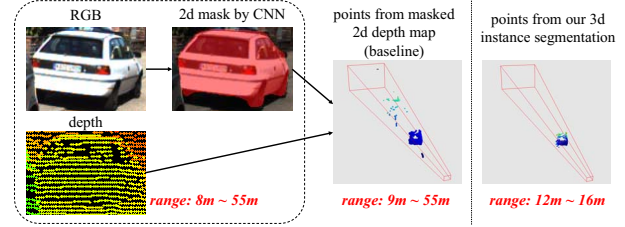


Figure 7. **Comparisons between 2D and 3D masks.** We show a typical 2D region proposal from KITTI val set with both 2D (on RGB image) and 3D (on frustum point cloud) instance segmentation results. The red numbers denote depth ranges of points.

5.3. Qualitative Results and Discussion

In Fig. 6 we visualize representative outputs of our frustum PointNet model. We see that for simple cases of non-occluded objects in reasonable distance (so we get enough number of points), our model outputs remarkably accurate 3D instance segmentation mask and 3D bounding boxes. Second, we are surprised to find that our model can even predict correctly posed *amodal* 3D box from partial data (e.g. parallel parked cars) with few points. Even humans find it very difficult to annotate such results with point cloud data only. Third, in some cases that seem very challenging in images with lots of nearby or even overlapping 2D boxes, when converted to 3D space, the localization becomes much easier (e.g. P11 in second row third column).

On the other hand, we do observe several failure patterns, which indicate possible directions for future efforts. The *first* common mistake is due to inaccurate pose and size estimation in a sparse point cloud (sometimes less than 5 points). We think image features could greatly help esp. since we have access to high resolution image patch even for far-away objects. The *second* type of challenge is when there are multiple instances from the same category in a frustum (like two persons standing by). Since our current pipeline assumes a single object of interest in each frustum, it may get confused when multiple instances appear and thus outputs mixed segmentation results. This problem could potentially be mitigated if we are able to propose multiple 3D bounding boxes within each frustum. *Thirdly*, sometimes our 2D detector misses objects due to dark lighting or strong occlusion. Since our frustum proposals are based on region proposal, no 3D object will be detected given no 2D detection. However, our 3D instance segmentation and amodal 3D box estimation PointNets are not restricted to RGB view proposals. As shown in the supplementary, the same framework can also be extended to 3D regions proposed in bird’s eye view.

Acknowledgement The authors wish to thank the support of Nuro Inc., ONR MURI grant N00014-13-1-0341, NSF grants DMS-1546206 and IIS-1528025, a Samsung GRO award, and gifts from Adobe, Amazon, and Apple.

References

- [1] Kitti 3d object detection benchmark leader board. http://www.cvlibs.net/datasets/kitti/eval_object.php?obj_benchmark=3d. Accessed: 2017-11-14 12PM. **2**
- [2] Kitti bird's eye view object detection benchmark leader board. http://www.cvlibs.net/datasets/kitti/eval_object.php?obj_benchmark=bev. Accessed: 2017-11-14 12PM. **2**
- [3] X. Chen, K. Kundu, Z. Zhang, H. Ma, S. Fidler, and R. Urtasun. Monocular 3d object detection for autonomous driving. In *Proceedings of the IEEE Conference on Computer Vision and Pattern Recognition*, pages 2147–2156, 2016. **2, 6**
- [4] X. Chen, K. Kundu, Y. Zhu, A. G. Berneshawi, H. Ma, S. Fidler, and R. Urtasun. 3d object proposals for accurate object class detection. In *Advances in Neural Information Processing Systems*, pages 424–432, 2015. **6**
- [5] X. Chen, H. Ma, J. Wan, B. Li, and T. Xia. Multi-view 3d object detection network for autonomous driving. In *IEEE CVPR*, 2017. **2, 5, 6**
- [6] Z. Deng and L. J. Latecki. Amodal detection of 3d objects: Inferring 3d bounding boxes from 2d ones in rgb-depth images. In *Conference on Computer Vision and Pattern Recognition (CVPR)*, volume 2, 2017. **2**
- [7] M. Engelcke, D. Rao, D. Z. Wang, C. H. Tong, and I. Posner. Vote3deep: Fast object detection in 3d point clouds using efficient convolutional neural networks. In *Robotics and Automation (ICRA), 2017 IEEE International Conference on*, pages 1355–1361. IEEE, 2017. **1, 2**
- [8] A. Geiger, P. Lenz, C. Stiller, and R. Urtasun. Vision meets robotics: The kitti dataset. *The International Journal of Robotics Research*, 32(11):1231–1237, 2013. **5**
- [9] A. Geiger, P. Lenz, and R. Urtasun. Are we ready for autonomous driving? the kitti vision benchmark suite. In *Conference on Computer Vision and Pattern Recognition (CVPR)*, 2012. **5**
- [10] R. Girshick, J. Donahue, T. Darrell, and J. Malik. Rich feature hierarchies for accurate object detection and semantic segmentation. In *Computer Vision and Pattern Recognition (CVPR), 2014 IEEE Conference on*, pages 580–587. IEEE, 2014. **1**
- [11] K. He, G. Gkioxari, P. Dollár, and R. Girshick. Mask r-cnn. *arXiv preprint arXiv:1703.06870*, 2017. **1, 4, 7**
- [12] M. Jaderberg, K. Simonyan, A. Zisserman, et al. Spatial transformer networks. In *NIPS 2015*. **4**
- [13] J. Lahoud and B. Ghanem. 2d-driven 3d object detection in rgb-d images. In *Proceedings of the IEEE Conference on Computer Vision and Pattern Recognition*, pages 4622–4630, 2017. **2, 7**
- [14] B. Li. 3d fully convolutional network for vehicle detection in point cloud. *arXiv preprint arXiv:1611.08069*, 2016. **2, 5, 6**
- [15] B. Li, T. Zhang, and T. Xia. Vehicle detection from 3d lidar using fully convolutional network. *arXiv preprint arXiv:1608.07916*, 2016. **2**
- [16] Y. Li, S. Pirk, H. Su, C. R. Qi, and L. J. Guibas. Fpnn: Field probing neural networks for 3d data. *arXiv preprint arXiv:1605.06240*, 2016. **2**
- [17] T.-Y. Lin, P. Dollár, R. Girshick, K. He, B. Hariharan, and S. Belongie. Feature pyramid networks for object detection. *arXiv preprint arXiv:1612.03144*, 2016. **3**
- [18] D. Maturana and S. Scherer. Voxnet: A 3d convolutional neural network for real-time object recognition. In *IEEE/RSJ International Conference on Intelligent Robots and Systems*, September 2015. **1, 2**
- [19] A. Mousavian, D. Anguelov, J. Flynn, and J. Kosecka. 3d bounding box estimation using deep learning and geometry. *arXiv preprint arXiv:1612.00496*, 2016. **2, 5**
- [20] C. R. Qi, H. Su, K. Mo, and L. J. Guibas. Pointnet: Deep learning on point sets for 3d classification and segmentation. *Proc. Computer Vision and Pattern Recognition (CVPR), IEEE*, 2017. **1, 2, 4, 5**
- [21] C. R. Qi, H. Su, M. Nießner, A. Dai, M. Yan, and L. Guibas. Volumetric and multi-view cnns for object classification on 3d data. In *Proc. Computer Vision and Pattern Recognition (CVPR), IEEE*, 2016. **1, 2**
- [22] C. R. Qi, L. Yi, H. Su, and L. J. Guibas. Pointnet++: Deep hierarchical feature learning on point sets in a metric space. *arXiv preprint arXiv:1706.02413*, 2017. **1, 2, 4, 5, 7**
- [23] S. Ren, K. He, R. Girshick, and J. Sun. Faster r-cnn: Towards real-time object detection with region proposal networks. In *Advances in neural information processing systems*, pages 91–99, 2015. **2, 5**
- [24] Z. Ren and E. B. Sudderth. Three-dimensional object detection and layout prediction using clouds of oriented gradients. In *Proceedings of the IEEE Conference on Computer Vision and Pattern Recognition*, pages 1525–1533, 2016. **2, 7**
- [25] G. Riegler, A. O. Ulusoy, and A. Geiger. Octnet: Learning deep 3d representations at high resolutions. *arXiv preprint arXiv:1611.05009*, 2016. **2**
- [26] K. Simonyan and A. Zisserman. Very deep convolutional networks for large-scale image recognition. *arXiv preprint arXiv:1409.1556*, 2014. **7**
- [27] S. Song, S. P. Lichtenberg, and J. Xiao. Sun rgb-d: A rgb-d scene understanding benchmark suite. In *Proceedings of the IEEE Conference on Computer Vision and Pattern Recognition*, pages 567–576, 2015. **1, 5, 7**
- [28] S. Song and J. Xiao. Sliding shapes for 3d object detection in depth images. In *Computer Vision—ECCV 2014*, pages 634–651. Springer, 2014. **2**
- [29] S. Song and J. Xiao. Deep sliding shapes for amodal 3d object detection in rgb-d images. In *Proceedings of the IEEE Conference on Computer Vision and Pattern Recognition*, pages 808–816, 2016. **2, 7**
- [30] H. Su, S. Maji, E. Kalogerakis, and E. G. Learned-Miller. Multi-view convolutional neural networks for 3d shape recognition. In *Proc. ICCV*, 2015. **1**
- [31] D. Z. Wang and I. Posner. Voting for voting in online point cloud object detection. *Proceedings of the Robotics: Science and Systems, Rome, Italy*, 1317, 2015. **2**
- [32] P.-S. Wang, Y. Liu, Y.-X. Guo, C.-Y. Sun, and X. Tong. O-cnn: Octree-based convolutional neural networks for 3d

- shape analysis. *ACM Transactions on Graphics (TOG)*, 36(4):72, 2017. 2
- [33] Z. Wu, S. Song, A. Khosla, F. Yu, L. Zhang, X. Tang, and J. Xiao. 3d shapenets: A deep representation for volumetric shapes. In *Proceedings of the IEEE Conference on Computer Vision and Pattern Recognition*, pages 1912–1920, 2015. 1, 2
- [34] Y. Xiang, W. Choi, Y. Lin, and S. Savarese. Data-driven 3d voxel patterns for object category recognition. In *Proceedings of the IEEE Conference on Computer Vision and Pattern Recognition*, pages 1903–1911, 2015. 2
- [35] S.-L. Yu, T. Westfechtel, R. Hamada, K. Ohno, and S. Tadokoro. Vehicle detection and localization on birds eye view elevation images using convolutional neural network. *2017 IEEE International Symposium on Safety, Security and Rescue Robotics (SSRR)*, 2017. 5, 6